

Processing Ultra Wide Band Synthetic Aperture Radar Data with Motion Errors

Søren Nørvang Madsen

Abstract—Several issues make the processing of ultra wide band (UWB) SAR data acquired from an airborne platform difficult. The character of UWB data invalidates many of the usual SAR batch processing techniques, leading to the application of wavenumber domain type processors. Additionally, strip mode SAR processors generally do not support motion compensation which is a function of the target location within the antenna beam. This paper will suggest and evaluate an algorithm which combines a wavenumber domain processing algorithm with a motion compensation procedure which enables motion compensation to be applied as a function of target range and the azimuth angle.

Keywords—Ultra Wide Band SAR, synthetic aperture radar, motion compensation.

I. INTRODUCTION

SYNTHETIC aperture radar (SAR) systems are imaging radars usually carried on an aircraft or a satellite. By transmitting pulses of electromagnetic energy while moving the radar system along a straight line (or a well defined arc), and receiving and processing the echoes from those pulses in a coherent manner it is possible to synthesize long antennas, and achieve very high image resolution. Descriptions of the basic principles of SAR are found in early references, e.g. [1], or in more recent books, e.g. [2] (note, many early references are found in a book by Kozuly, [3]). Familiarity with the basic SAR principles will be assumed in the following.

A. Long wavelength phenomenology

Lately there has been a increased interest in developing SAR systems that operate at long wavelengths and at the same time achieve very high resolution in both range and azimuth. There are many reasons for this interest. Generally, increasing the wavelength leads to a larger penetration depth. This was dramatically demonstrated when the first L-band Shuttle Imaging Radar, SIR-A, in 1981 showed that a 24 cm wavelength SAR could penetrate several meters of dry desert sand, [4]. Also, the phenomenology of the scattering at the larger wavelengths is quite different from that of more common centimeter level wavelengths. Many natural targets (e.g. fields, plains, water) are smooth at these wavelengths while other targets will appear very bright (e.g. targets resonating with the long wavelength or double bounce reflections) resulting in images which appear as a very dark background with bright point scatterers

spread out over the scene. The justifications for the interest in the simultaneous high resolution in both range and azimuth includes, 1) the requirement for high resolution (e.g. for target identification, military applications); 2) a desire to avoid the speckle phenomenon (which is caused by the resolution cell being wide relative to half the wavelength); and 3) the added information in illuminating a target with a broadband signal as the target scattering properties can/will change over the bandwidth.

B. Systems

A number of systems have been designed to collect long wavelength SAR imagery. The JPL AIRSAR system, [5], has included a long wavelength $\lambda = 0.7$ m UHF channel since 1987. The purpose of this system is primarily to study the phenomenology at L-, L-, and C-band to build a knowledge base relevant to the design of spaceborne systems. The spatial resolution requirement for this system is therefore quite moderate. One of the first systems to operate at long wavelengths while simultaneously achieving high resolution was developed by SRI. This system use an impulse excitation which generates a transmitted spectrum extending from 100 to 600 MHz, and images processed to 200 MHz bandwidth were demonstrated in [6]. The Environmental Research Institute of Michigan (ERIM) has recently built a wideband UHF upgrade to the NAWC/ERIM P-3 SAR system. This system was first tested in December of 1994. The primary application of this system is to study penetration of foliage and the detection and classification of cultural objects. To meet these objectives and to be useful for other remote sensing applications this system has been designed with a very high resolution, 0.33 m in range and 0.66 m in azimuth. This system has a 500 MHz instantaneous bandwidth that can be selected within the total frequency range of 200-900 MHz. The Swedish CARABAS utilizes even longer wavelengths as it operates in the band from 20 to 90 MHz, [7] (this reference lists a number of active UHF/VHF radar programs, and includes a discussion of the reasons for applying longer wavelengths). Other active UWB programs are also discussed in [8].

C. Long wavelength interferometry

An important motivation for the work described here is recent considerations at JPL concerning the development of a long wavelength interferometric SAR. SAR interferometry relies on combining two SAR images coherently. Assuming that two SAR antenna tracks are located such that each target element in the SAR images is observed at slightly different elevation angles, the two data sets can

This work was performed at the Jet Propulsion Laboratory, California Institute of Technology, under contract with the National Aeronautics and Space Administration.

The author is with the Jet Propulsion Laboratory, California Institute of Technology, Pasadena, CA 91109. E-mail: snm@jpl.nasa.gov

be used to derive a highly accuracy 3-dimensional map of the observed scene. The theory of SAR interferometry is discussed in [9], [10], [11]. Processing techniques for interferometric systems operating in the microwave range of the spectrum have already been developed, [12] and [13], and height resolutions on the order of a few meters have been demonstrated, [14]. If the scene being mapped is covered by dense vegetation, centimeter wavelength interferometric systems largely observe the top portion of a canopy, and as the ground level is the desired height for topographic mapping an undesired bias vegetation can be induced. Knowing that longer wavelengths penetrate foliage better, it is obviously worth considering, if an interferometric SAR operating at long wavelengths, UHF or VLF, could provide a more accurate estimate of the true ground height. This evaluation is complex and involves many critical issues. One of the key issues is whether it is possible to develop an efficient processing algorithm which provides sufficient accuracy with respect to phase fidelity and geometric accuracy for interferometric applications. That is the subject of this paper.

D. Outline

Section 2 will present the processing requirements in more detail and outline the shortcomings of existing algorithms. In section 3 the basic equations of the wave-domain processing approach are summarized and these equations will be the basis of the following sections. Section 4 will augment the basic processing equations with modifications describing broadside motion compensation, and this lead to the second order motion compensation correction which is derived in section 5. This is followed by a description of a simulation system developed and presentation of simulation results, section 6. Section 7 discusses limitations of the proposed algorithm, followed by the conclusion of the paper, section 8.

1]. UWB PROCESSING ISSUES

The processing of strip-map L/J11 data acquired from an aircraft involves at least two complications. First, even in the ideal case where an aircraft is flying along a perfectly straight line, the wide range of wavelengths spanned by the bandwidth invalidates a number of approximations which are used in the standard SAR processors. The much used range-Doppler processor, for instance, relies on the range migration being a function of the Doppler frequency as the range migration is given by the off-boresight angle and, for a given wavelength, the Doppler frequency is also a function of the off-boresight angle. However, this approach will fail in the UWB case as the wavelength is not well defined. An excellent examination of errors introduced by the approximations of several well known processing schemes is found in [15]. However, the so-called wavenumber domain algorithm, originally proposed by Rocca, [16], [17], [15], is well suited. The second complication is that the beamwidth of a UWB system has to be very large (on the order of one radian) for the range and azimuth resolutions

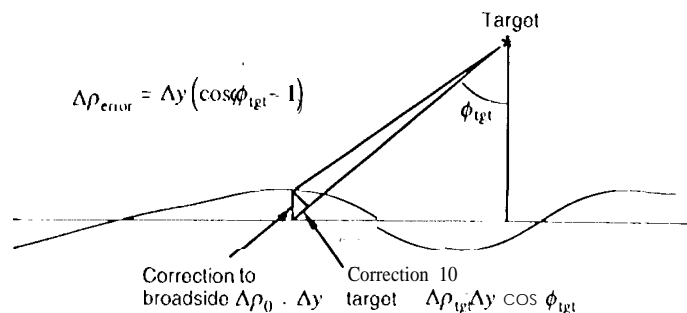


Fig. 1. The difference between the across-track motion displacement, (= broadside correction) and the displacement to an off-broadside target, viewed in the slant range plane.

to be comparable. This is realized by observing that, the slant range resolution is

$$\delta \rho = \frac{c}{2B}$$

(c is the speed of light, B is the range bandwidth) and the azimuth resolution for a given frequency and change in aspect angle is approximately, [1],

$$\frac{\lambda}{4 \sin \theta/2} = \frac{c}{4f \sin \theta/2}$$

and since f is not much larger than B in a UWB system then θ must be on the order of one radian for the range and azimuth resolutions to be comparable.

The motion compensation problem is illustrated in Fig. 1. In this slant range projection it is seen that if the angle to the target differs from the direction assumed in the motion compensation then an error

$$\Delta \rho_{moc} = \Delta y (\cos \phi_{tgt} - \cos \phi_{moc})$$

is introduced. In the broadside case the error is

$$\Delta \rho_{moc} = \Delta y (\cos \phi_{tgt} - 1)$$

Before the azimuth compression each range line will include reflections from all targets covered by the width of the antenna beam. One approach to improve the motion compensation degree for angles deviating from the antenna fan beam plane is to combine a spot-like type motion compensation scheme, with a stripmap processing algorithm as suggested in [18] and illustrated in Fig 2. This approach ensures that points close to the central reference point are correctly motion compensated for all aspect angles. The problem with this approach is that it requires the processing of a full aperture but will only provide good motion compensation in a small neighborhood of the reference point. As the ratio between the patch length which needs to be processed and the useful image patch is very large for typical system parameters, this algorithm is less attractive from an efficiency point of view.

To illustrate principles, system parameters as shown in Table I are assumed in the following. Phase accuracy requirements are addressed first. A coarse calculation shows

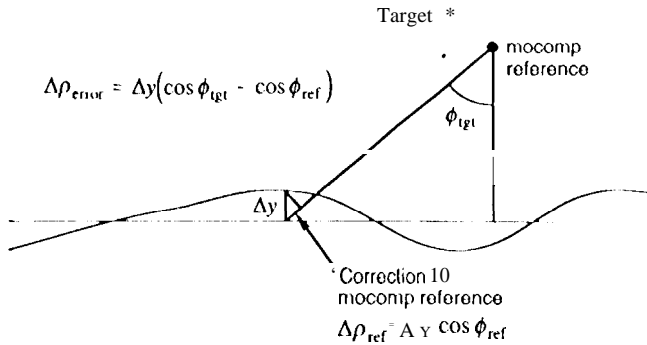


Fig. 2. Motion compensation optimized with respect to a central reference point in the scene.

that for a 10 m horizontal interferometric baseline (transmit and receive on same antenna, single pass or repeat pass) a desired height accuracy of 2 m, equivalent to a 2.8 m cross-line-of-sight error (at 45° angle of incidence), scaled by an approximately 7 m orthogonal baseline relative to a 15 km slant range, gives a maximum error of 1.3 mm on the slant range measured by the interferogram. This is equivalent to 0.7° (12 mrad) of phase error on either channel (assuming the channel errors are independent, which is not necessarily right but it provides an order of magnitude for the accuracy sought). An approximate expression for the residual phase error when a spotlike type motion compensation is applied was derived in [18],

$$\Phi_c = -\frac{\pi W_a^2}{2(\rho_0 - \frac{W_r}{2})^2} \Delta y \cos^3 \phi$$

Φ_c is the residual phase error, ρ_0 is the range to the center of the patch, W_a, W_r are the azimuth and range extents of the patch, Δy is the off-set, from the actual track to the desired track, and ϕ is the off-boresight angle. Using the parameters of Table 1, and assuming the range extent of the patch to be zero, the azimuth extent of each patch needs to be smaller than approximately 600 m. This compared to the aperture length of 750010 means that 8100 m along-track needs to be processed to advance the processing by 600 m, thus the input data must be processed 13.5 times on the average. When actual slant range extent is taken into account the efficiency of the spotlike motion compensation technique degrades further.

A second requirement is particularly important for repeat-track interferometry, where the motion to be compensated for the two channels is completely independent. The geometry of the processed images should be so well defined that it is possible to overlay the two images and obtain a coregistration accuracy which is a fraction (typically on the order of a tenth) of the resolution cell size. This, however, is a less stringent requirement than the above phase accuracy requirement for the parameters assumed here. In a repeat-track situation, where the baseline is much larger, and the phase requirement correspondingly much relaxed, the geometrical requirement can be a factor.

In this paper it is assumed that the radar is transiting

TABLE I
ASSUMED SYSTEM PARAMETERS

Parameter	value
Center frequency	300 MHz
Bandwidth	200 MHz
Altitude	10 km
Slant range	15 km
Azimuth resolution	1 m
Aperture Length	7500 In
Aperture angle	28°
Maximum off-track deviation Δy	5 m

pulses with a uniform along-track spacing. Even when this is not the case it is a fairly simple matter to implement a variable rate azimuth presummer which effectively resamples the echo lines such that the output of the presummer will be uniformly spaced.

III. THE BASIC IDEA

The key dilemma in properly correcting for undesired motion, in a wide beam system, is that one needs to know and track the target location which is, however, not known from the outset, for a wide area strip map system. The basic idea to be employed in the algorithm suggested here is: 1) To perform a first level of processing with some nominal motion compensation applied, thus partially focussing the image, and 2) to reprocess individual subpatches of this image to refine the motion compensation correction. In step one of this processing it is assumed that the target is in the antenna fan beam plane. Targets are therefore *not* motion compensated correctly in off-boresight directions, however, the motion compensation in the beam center direction is correct. This will ensure that the target impulse responses are located correctly geometrically even though generally insufficiently focussed. In step two of the processing, the target location is defined by the center of the subpatch to be reprocessed, and it is thus a key requirement that the reprocessing per output patch is much less computationally demanding than the first processing of the wide area patch such that it is computationally affordable to reprocess many small patches. As only the center of each subpatch is processed correctly a small subpatch size is important to the performance.

IV. THE WAVENUMBER DOMAIN PROCESSOR

To facilitate the derivations to come in the following sections, and to establish the notation, this section will summarize the key equations of the wavenumber domain processor. Note that the processor could equally well have been called the frequency domain processor. In the following derivations are expressed in terms of the spatial frequencies in both range and azimuth.

Consider the geometry shown in Fig 3. The x and y coordinates refers to the along-track and across-track target/scatterer coordinates and the X and ρ coordinates refer to

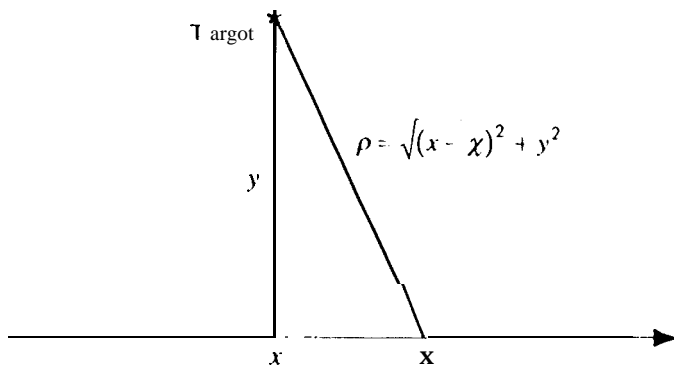


Fig. 3. SAR slant range plane geometry.

the image coordinates. The across-track coordinates are slant plane coordinates.

The complex valued baseband received signal, $ss(\rho, \chi)$, is

$$ss(\rho, \chi) = \iint A \left(\frac{x - \chi}{y} \right) \frac{g(x, y)}{R^p} h(\rho - R) \exp \left\{ -j \frac{4\pi}{\lambda_0} R \right\} dx dy \quad (1)$$

where A accounts for the azimuth antenna pattern, g is the complex backscatter, R^p represents the signal attenuation with range ($p = 4$ if the antenna illumination is uniform ill range!), h is the complex baseband representation of the transmitted signal's range modulation, and

$$R = R(x, \chi, y) = \sqrt{(x - \chi)^2 + y^2}$$

is the slant range. Substituting $f_{\rho 0} = \frac{2}{\lambda_0} = \frac{2f_0}{c}$ for the slant range spatial frequency carrier, followed by a Fourier transform in range and azimuth, leads to,

$$\begin{aligned} SS(\hat{f}_\rho, f_\chi) &= \iiint A \left(\frac{x - \chi}{y} \right) \frac{g(x, y)}{R^p} h(\rho - R) \\ &\quad \exp \{ -j 2\pi f_{\rho 0} R \} dx dy \\ &\quad \exp \left\{ -j 2\pi \left(\rho \hat{f}_\rho + \chi f_\chi \right) \right\} d\rho d\chi \\ &= H(\hat{f}_\rho) \iiint A \left(\frac{\chi}{y} \right) \frac{g(x, y)}{\sqrt{\kappa^2 + y^2}} \\ &\quad \exp \left\{ -j 2\pi \left(f_\rho \sqrt{\kappa^2 + y^2} + f_\chi \kappa + f_\chi x \right) \right\} \\ &\quad d\kappa dx dy \end{aligned} \quad (2)$$

where the spatial frequency is the sum of the carrier frequency and the baseband frequency, $f_\rho = f_{\rho 0} + \hat{f}_\rho$, and $\kappa = \chi - x$ is the difference between the target and observation along-track positions.

The range compression is irrelevant for this discussion, and trivial, as it can be performed on each individual line before performing the azimuth compression. For simplicity the range transfer function, $H(f_\rho)$, in equation (3) is thus assumed to be a real valued range spectral weighting function of the range signal *after* range compression,

Before continuing, it is also noted that usually the range Fourier transform is performed with respect to some off-set range, $\tilde{\rho} = \rho - \rho_0$, and from (2) it is seen that the Fourier transform evaluated at an off-set range is obtained by multiplying by the exponential term, $\exp \{ j 2\pi f_\rho \tilde{\rho}_0 \}$.

The stationary phase approximation, [19],

$$\begin{aligned} \int f(\kappa) \exp \{ j r \# (\kappa) \} d\kappa \\ \approx f(\kappa_0) \sqrt{\frac{2\pi}{j \phi'(\kappa_0)}} \exp \{ j \phi(\kappa_0) \} \quad (4) \\ \phi'(\kappa_0) = 0 \end{aligned}$$

is a useful approximation as the azimuth time-bandwidth for relevant radar cases is large. Noting that the phase function is

$$\phi(\kappa) = -2\pi(f_\rho \sqrt{\kappa^2 + y^2} + f_\chi \kappa) \quad (5)$$

and the stationary phase point is

$$\kappa_0 = -\frac{f_\chi}{\sqrt{f_\rho^2 - f_\chi^2}} y \quad (6)$$

(3) becomes after applying the stationary phase approximation,

$$\begin{aligned} \bar{SS}(\hat{f}_\rho, f_\chi) &= \exp \{ j 2\pi \hat{f}_\rho \rho_0 \} H(\hat{f}_\rho) A \left(\frac{f_\chi}{\sqrt{f_\rho^2 - f_\chi^2}} \right) \\ &\quad \iint \frac{g(x, y)}{y^{p-1/2}} \exp \left\{ -j 2\pi \left(f_\chi x + y \sqrt{f_\rho^2 - f_\chi^2} \right) \right\} dx dy \end{aligned} \quad (7)$$

where \bar{SS} is the Fourier transform taken with respect to the off-set slant range and scaled as

$$\begin{aligned} \bar{SS}(\hat{f}_\rho, f_\chi) &= \exp \{ j 2\pi \hat{f}_\rho \rho_0 \} SS(\hat{f}_\rho, f_\chi) \\ \bar{SS}(\hat{f}_\rho, f_\chi) &= \bar{SS}(\hat{f}_\rho, f_\chi) \sqrt{-j f_\rho^{-1} (f_\rho^2 - f_\chi^2)^{3/4 - p}} \end{aligned}$$

At this point it is obvious that by making the substitution]

$$f_y = f_{y0} + \hat{f}_y = \sqrt{f_\rho^2 - f_\chi^2} = \sqrt{(f_{\rho 0} + \hat{f}_\rho)^2 - f_\chi^2}$$

the inverse Fourier transform of $GG(\hat{f}_y, f_\chi) = \bar{SS}(\hat{f}_\rho, f_\chi)$, times $y^{p-1/2}$, provides a bandpass-filtered version of $g(x, y)$ with the filtering defined by H and A .

Finally taking into account the range offset of the output image $\hat{y} = y - y_0$ and formulating the result in terms of baseband frequencies, $\hat{f}_y = f_y - f_{y0}$, provides

$$\begin{aligned} \bar{GG}_0(\hat{f}_y, f_\chi) &= \bar{SS}(\hat{f}_\rho, f_\chi) \exp \left\{ -j 2\pi \hat{f}_\rho \rho_0 \right\} \exp \left\{ j 2\pi \hat{f}_y y_0 \right\} \\ &= H(f_\rho) A \left(\frac{f_\chi}{f_{y0} + \hat{f}_y} \right) \iint \frac{g(x, y) \exp \left\{ -j 2\pi y f_{y0} \right\}}{y^{p-1/2}} \\ &\quad \exp \left\{ -j 2\pi \left(f_\chi x + \hat{f}_y \hat{y} \right) \right\} dx dy \end{aligned} \quad (8)$$

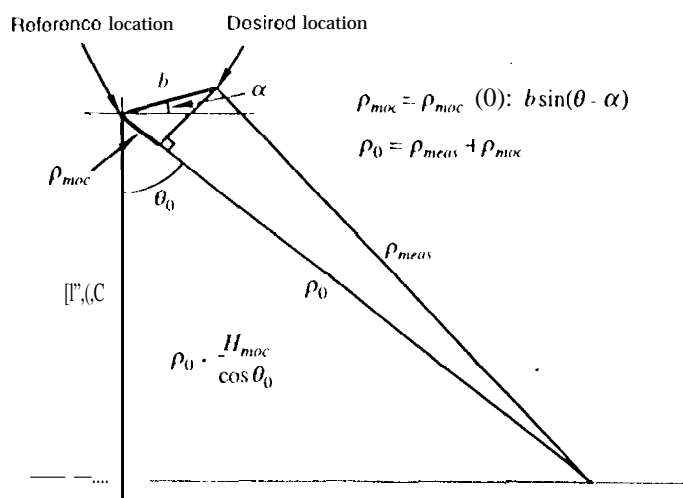


Fig. 4. The motion compensation geometry in the fan beam plane.

$\tilde{G}G_0$ is the Fourier transform of $g(x,y)/y^{p-1/2}$ and the index zero is indicating that the resampling scheme applied does not take motion compensation into account.

V. FIRST ORDER MOTION COMPENSATION

A first order motion compensation, which can be applied independently of the azimuth processing, assumes that all targets are in the antenna fan beam plane and that all targets are at a reference elevation, such that the effective platform elevation is H_{moc} . For side-looking UWB systems, the fan beam plane is generally so wide that it will be assumed to be in the broadside direction. This does not limit the principles applied and it does simplify the mathematical presentation to follow.

The motion compensation geometry is presented in Fig 4.

It will be useful in the following to note that in any point the correction applied by this first order motion compensation is equivalent to a phase shift defined by the motion-off-set in the line-off-sight direction, k , and a frequency shift defined by the motion off-set in the cross-line-off-sight direction, l , as

$$\begin{aligned}\rho_{moc} &= b \sin(\theta - \alpha) \\ &\approx b \sin(\theta_0 - \alpha) + \frac{b \cos(\theta_0 - \alpha)}{\rho_0 \tan \theta_0} (\rho - \rho_0) \\ &\approx k(\chi) + \frac{l(\chi)}{\rho_0 \tan \theta_0} (\rho - \rho_0)\end{aligned}\quad (9)$$

$$\begin{aligned} k(\chi) &= b \sin(\theta_0 - \alpha) \\ l(\chi) &= b \cos(\theta_0 - \alpha) \end{aligned} \quad (10)$$

The expansion is defined by ρ_0 , the radar displacement given by 11 and α , and the assumed target height, H_{moc} .

To implement this first order motion compensation, the received and rail.gc compressed signal $ss(\rho, \chi)$ is interpolated in range and phase shifted,

$$ss_{moc}(\rho, \chi) = ss_{meas}(\rho - \rho_{moc}, \chi) \exp \{-j2\pi f_{\rho 0} \rho_{moc}\} \quad (11)$$

VI. SECOND ORDER MOTION COMPENSATION

In this section it is calculated how the actual platform motion relative to the target as well as the applied first order motion compensation affects the basic equations establishing the wavenumber domain processing approach. As the results will be target dependent it is reiterated that the basic idea of this processing scheme is to first process the data, after application of the first order motion compensation, using the basic algorithm described in section IV. Then small patches from the image are extracted, and Fourier transformed, thus the approximate target locations are known, basically with an uncertainty which is half the window size. The implications of this error is discussed in a following section.

The starting point for the derivation is (11) and the observation that the slant range is now given by

$$\begin{aligned}
 R &= R(\chi) = \sqrt{(x - \chi)^2 + (y - \Delta y(\chi))^2} \\
 &\approx \sqrt{(x - \chi)^2 + y^2} - \frac{y \Delta y(\chi)}{\sqrt{(x - \chi)^2 + y^2}} \\
 R_0(\chi) &= \frac{y \Delta y(\chi)}{R_0(\chi)} \quad (12)
 \end{aligned}$$

It is noted that Δy is the true motion deviation whereas the earlier defined k and 1 deviations are values assumed in the motion compensation. To keep the description to a minimum in this section, it is noted that in the derivation of the simple wavenumber domain processor the integrations over x and y were carried over throughout the calculation. These integrals are therefore left out in the following, but are implicitly assumed. Similarly the weighting function in azimuth, $A(\dots)$, does not change compared to the simple treatment and is thus ignored.

Describing the motion compensated signal in terms of the linear expansion in k and 1 provides

$$ss_{moc}(\rho, x) = h \rho R - k(x) \frac{l(x)}{\rho_0 \tan \theta_0} (\rho - \rho_0) \exp \left\{ -j2\pi f_{\rho_0} \left(k(x) + \frac{l(x)}{\rho_0 \tan \theta_0} (\rho - \rho_0) \right) \right\} \frac{g(x, y)}{R^p} \exp \{ -j2\pi f_{\rho_0} R \} \frac{A(x)}{R^p} \left(\frac{\rho}{\rho_0} \right)^{1 - \frac{l(x)}{\rho_0 \tan \theta_0}} R'(x) \exp \left\{ -j2\pi f_{\rho_0} \frac{l(x)}{\rho_0 \tan \theta_0} \rho \exp \{ -j2\pi f_{\rho_0} R' \} \right\} R'(x) = R_0(x) - \frac{y \Delta y(x)}{R_0(x)} - k(x) \frac{l(x)}{\tan \theta_0}$$

At this point the Fourier relationship

$$h(\alpha\rho - \beta)\exp(-j\gamma\rho) \stackrel{\text{Fourier}}{\longleftrightarrow} \frac{1}{\alpha} \exp\left\{-j2\pi\frac{f+\gamma}{\alpha}\right\} H\left(\frac{f+\gamma}{\alpha}\right) \quad (14)$$

is used to arrive at the range frequency, azimuth space result given in Appendix A, which to first order in the

motion perturbations is equal to

$$SS_{moc}(\tilde{f}_\rho, \chi) \approx \frac{g(x, y)}{R^p} H \left(\tilde{f}_\rho + f_\rho \frac{l(\chi)}{\rho_0 \tan \theta_0} \right) \exp \left\{ -j2\pi f_\rho \left(1 + \frac{l(\chi)}{\rho_0 \tan \theta_0} \right) R'(\chi) \right\} \quad (15)$$

Performing the azimuth Fourier transform provides

$$SS_{moc}(\tilde{f}_\rho, f_\chi) = \int \frac{g(x, y)}{R^p} H(\dots) \exp \{ j\phi(\kappa) \} \exp \{ -j2\pi f_\chi x \} d\kappa \quad (16)$$

$$\phi(\kappa) = -2\pi \left(f_\rho \left(1 + \frac{l(\kappa + x)}{\rho_0 \tan \theta_0} \right) R'(\kappa + x) - f_\chi \kappa \right) \quad (17)$$

By expressing the stationary phase solution, $\hat{\kappa}$, in terms of the perturbation, $\tilde{\kappa}$, to the solution when no motion is present as $\hat{\kappa} = \kappa_0 + \tilde{\kappa}$, the first order solution is easily found (see Appendix B). It is noted, that for the actual system parameter combinations studied (see Simulations below) the first order motion compensation will stabilize the image geometry so well that ignoring $\tilde{\kappa}$ is of minor consequence. The modified stationary point is denoted $\hat{\kappa}$ in the following.

Multiplying out the expressions for the phase, (17), to first order in the motion perturbations leads to:

$$\phi(\kappa) \approx -2\pi \left(f_\rho R_0(\hat{\kappa}) - f_\chi \hat{\kappa} - f_\rho \varepsilon \right) \quad (18)$$

with ε given by

$$\varepsilon = \frac{\varepsilon(\hat{\kappa}, x, y, \rho_0)}{R_0(\hat{\kappa})} = \frac{l(\hat{\kappa} + x) R_0(\hat{\kappa}) - \Delta y(\hat{\kappa} + x)}{\rho_0 \tan \theta_0 - y} - \frac{k(\hat{\kappa} + x)}{y} - \frac{l(\hat{\kappa} + x)}{y \tan \theta_0} \quad (19)$$

Note that κ_0 is a stationary point for $f_\rho R_0(\kappa) + f_\chi \kappa$. Thus the desired Fourier relation

$$\tilde{SS}(\tilde{f}_\rho, f_\chi) \approx \exp \{ j2\pi \tilde{f}_\rho \rho_0 \} H(\dots) \frac{g(x, y)}{y^{p-1/2}} \exp \{ -j2\pi (f_\chi x + f_y y) \} \quad (20)$$

is established if f_y and f_ρ are defined as:

$$f_y = \sqrt{f_\rho^2 - f_\chi^2} + \varepsilon f_\rho \quad (21)$$

$$f_\rho \approx \sqrt{f_y^2 + f_\chi^2} - \varepsilon f_y \quad (22)$$

The final result which will define the proposed algorithm is obtained by observing that the Fourier transform of $g(x, y)/y^{p-1/2}$ when motion compensation is taken into account, can be expressed in terms of the algorithm applied when motion compensation is *not* taken into account, as

$$\begin{aligned} \tilde{GG}(\tilde{f}_y, f_\chi) &= \tilde{SS}(\sqrt{f_y^2 + f_\chi^2} - f_y \varepsilon - f_\rho, f_\chi) \\ &\exp \left\{ -j2\pi \left(\sqrt{f_y^2 + f_\chi^2} - f_y \varepsilon - f_\rho \right) \rho_0 \right\} \\ &\exp \{ j2\pi \tilde{f}_y y_0 \} \\ &\approx \tilde{GG}_0(\tilde{f}_y + \partial f_y, f_\chi) \exp \{ -j2\pi \partial f_y y_0 \} \end{aligned} \quad (23)$$

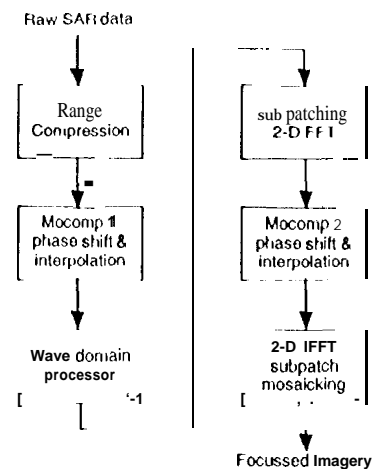


Fig. 5 Processing algorithm, block diagram

where the required frequency shift is given by,

$$\partial f_y = -\varepsilon \sqrt{(f_{y0} + \tilde{f}_y)^2 + f_\chi^2} \quad (24)$$

These many calculations therefore leads to the very simple result that a second order motion correction can be achieved by implementing a frequency domain shift and a corresponding phase shift to the frequency domain representation of the simple wavenumber domain algorithm.

VI. IMPLEMENTATION OF THE PROCESSOR

The basic flow of data through the processor is illustrated in Fig. 5. First the data is range compressed on a line by line basis. The range compression is followed by the motion compensation in the broadside (fan beam plane) direction. This step, mocomp 1, implements the interpolation and the phase shift of equation (11). The following processing step implements a wavenumber domain processor as detailed in section IV. This provides a partially focussed image. This partially focussed image is now subdivided into overlapping patches. For this study a patch overlay of 50% has been applied in both range and azimuth, see Fig. 5.

After dividing the image into subpatches each subpatch is 2-D Fourier transformed. The next processing step then implements the second order motion compensation given by equations (23-24). Note that at this point the target coordinates, x and y , are approximated by the center of the patch. Following the frequency domain interpolation and phase shift, the subpatch is inverse Fourier transformed, and the valid points of each subpatch are mosaicked to form the focussed image.

VIII. SIMULATIONS AND REVALUATION

The algorithm described in this paper has been tested with simulated data. A software suite was developed including three major modules:

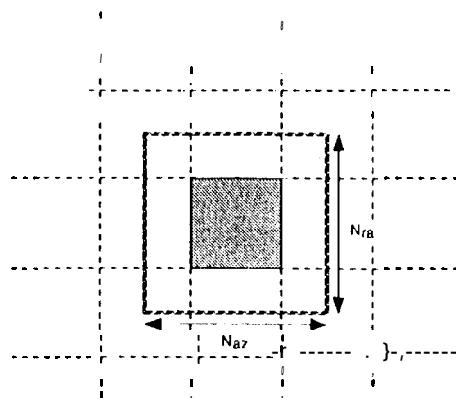


Fig. 6. Subpatch overlay.

TABLE 11
MOTION PARAMETERS

Parameters			
component	amplitude	period	phase
c_1	30 In	50 km	0.78 rad
c_2	2.5111	2.5 km	0 rad
h_1	0.5 m	1 km	1.57 rad

1. Raw Data Simulator. This module implements a spatial domain raw data simulator. The radar platform trajectory is defined by an arbitrary number of sinusoidal elements. Across-track and vertical motion is specified individually. The simulator is of the point target type. The 3-D locations of all targets are specified. The simulator also allows the specification of standard system parameters including, pixel spacing, bandwidth etc. The simulator implements an antenna beamwidth which is a function of frequency.
2. The wave domain processor. This module implements the first order motion compensation and a wavenumber domain processor.
3. Mocomp 2 processor. This module implements the second order motion compensation scheme. The patch size of the second order motion compensation correction can be varied.

A number of different geometries was simulated including parameters corresponding to fairly short range very high resolution systems as well as parameters representative of the proposed GEOSAR system. The simulation results presented here were based on the system parameters shown in Table I except for the motion parameters. The motion parameters are specified in Table 11, where c components indicate across-track motion, and the h component is vertical motion. The range and azimuth pixel spacings used in the simulations were 0.6 m and 0.8 m. A swath corresponding to 8192 range samples was simulated.

First it is noted, that the level of motion perturbations simulated here are so large that without motion compen-

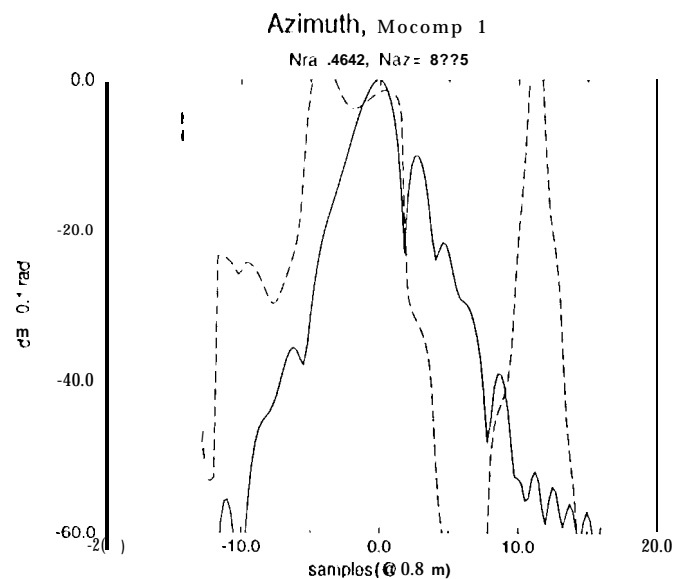


Fig. 7. Impulse response function, in azimuth, when first order motion compensation is applied. Solid line is amplitude in dB, the dashed line is 10 times the phase in radians.

sation no well defined mainlobe is obtained at all (most of the signal energy is spread out over a 60-70 m irregular impulse response function in the azimuth dimension). Range impulse response functions are not discussed at all in the following as the azimuth impulse response function is a much more sensitive indicator of performance.

A typical azimuth impulse response after processing with the first order motion compensation is shown in Fig. 7. The solid line indicated the amplitude response in dB, the dashed line shows the phase response multiplied by ten. A quite irregular impulse response function is noted, and the phase variation over the mainlobe is clearly unacceptable for interferometric applications.

In Fig. 8 is shown the same point target, however, after the second order motion compensation has been applied. Note that in this case the phase plotted is the actual phase multiplied by 100. This plot is a best case situation in the sense that the point target was located in the center of the patch in the azimuth direction. (It is noted that for range patch sizes 512 range bins or smaller, range location was insignificant for the results.)

Figs. 9 and 10 are on the other hand worst case situations as the patch boundary in this case was going right through the mainlobe of the impulse response function. In Figs. 9 the target peak is immediately after a patch boundary which means that the patch center is located half the patch width after this impulse response function.

In Figs. 10 the target peak is immediately before a patch boundary which means that the patch center is located half the patch width before this impulse response function. It was interesting to note that the actual phase at the peak did vary as a function of the patch location relative to the target location. Ideally, the patch center and the target location should be identical. For these simulations it was

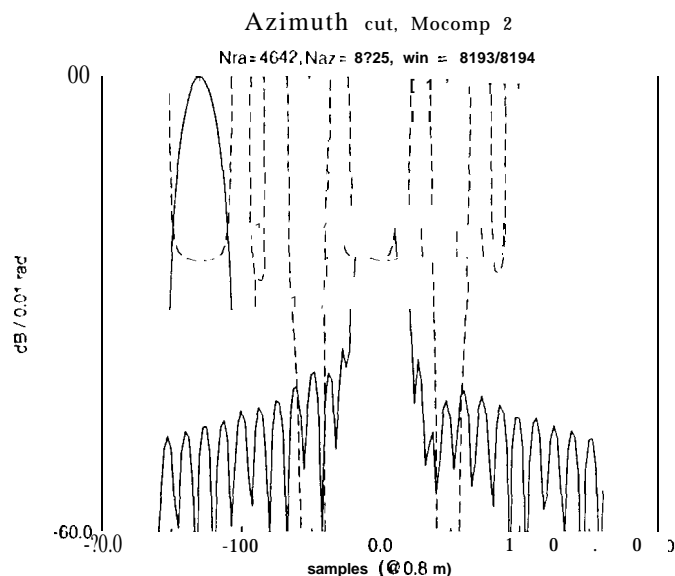


Fig. 8. Impulse response function, in azimuth, when second order motion compensation is applied. The target is centered in the reprocessed patch. Solid line is amplitude in dB, the dashed line is 100 times the phase in radians.

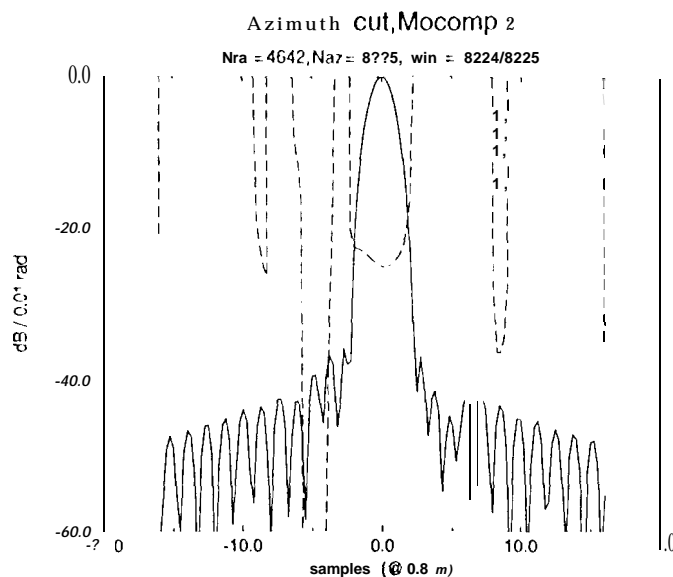


Fig. 9. Impulse response function, in azimuth, when second order motion compensation is applied. The target peaks immediately after the transition from one patch to the next. Solid line is amplitude in dB, the dashed line is 100 times the phase in radians.

found that the phase at the peak varied from 0.244 radians in the "center" case, to 0.238 and 0.251 in the "before" and "after" cases. This variation of ± 0.07 radians was observed with an azimuth patch size of 128 samples (of which the central 64 samples are kept). Tests using patch sizes of 256 and 512 samples showed that the phase error at the peak scaled with the distance from the point target to the center of the patch (as expected).

IX. LIMITATIONS

The algorithm does have limitations which should be noted. Two of these limitations relate to the sensitivity to target location within the swath as indicated in the previous section.

Due to the fact that the target location is approximated by the center of the subpatch processed, the motion compensation data applied for the second order motion compensation can be offset by a quarter of the patch size in the along-track direction. This basically means that, high frequency motion will not be corrected as well as low frequency components. Some simple trigonometric calculations will show that for an along-track offset, Δx , the attenuation of a motion perturbation with period e is

$$2 \sin \frac{\pi \Delta x}{e}$$

which also shows that for motion periods shorter than 6 times the worst case along-track offset (equal to one quarter of the patch size) the second order motion compensation can actually result in a impulse response degradation. These higher frequency components should thus be removed from the motion data before second order motion compensation is applied.

The second performance issue is the phase discontinuity on patch boundaries. The discontinuity observed in the simulation results presented above can be explained by the 64 sample shift of the motion perturbations. A theoretical calculation will show that taking into account that the second order motion compensation is proportional to $\cos \phi$, where ϕ is the off-boresight angle, then the slope of the 30 km period perturbation will introduce a worst-case phase discontinuity of 0.08 radians, in good agreement with the simulation results.

In the simulations shown here the height difference between the radar platform and the target assumed in the motion compensation was identical to the height difference applied in simulating the raw data. In real life unknown target topography will introduce differences between the actual height and the assumed height. Additional simulations showed that even fairly small errors in the assumed height would severely degrade the impulse response function. The degradations observed were in good agreement with simple theoretical calculation of the error introduced in the assumed line-of-sight direction when the assumed target height is in error. This reduction in the motion compensation degree caused by uncertainties in the target elevation is *not* related to the algorithm applied but is a fundamental problem, which would also exist even if a time-domain processor was applied. However, the fact that the second order motion compensation is implemented as an additional processing step following the standard wavenumber domain processing does make it possible to iterate the second order motion compensation as topographic information becomes available in an interferometric system.

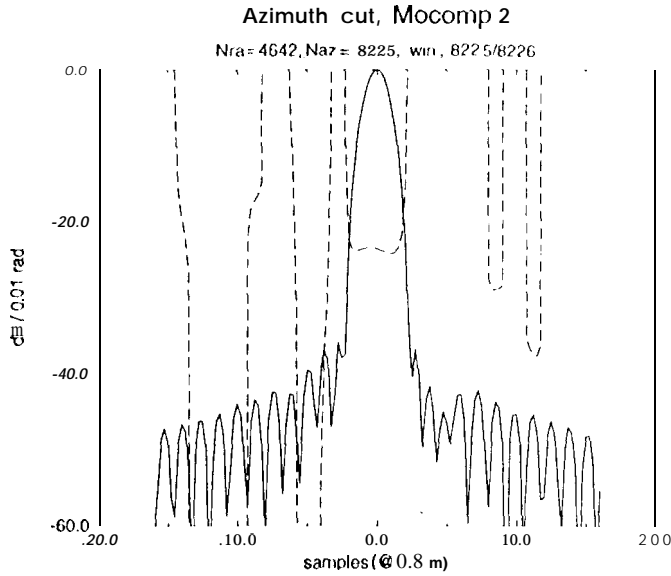


Fig. 10. Impulse response function, in azimuth, when second order motion compensation is applied. The target peaks immediately before the transition [f-0il] one patch to the next. Solid line is amplitude in dB, the dashed line is 100 times the phase in radians.

X. CONCLUSIONS

This paper outlines a processing algorithm which will process ultra wide band synthetic aperture radar data perturbed by undesired radar platform motion. The algorithm will account for motion deviations as a function of the changing relative position of the target within the antenna beam over the aperture formation. The algorithm is computationally very efficient, compared to both a time-domain processor and other published processing schemes applicable to this problem.

XI. APPENDIX A.

The range Fourier transform of (13) when using the Fourier relation given in (14) is

$$S_{smoc}(\hat{f}_p, \chi) = \frac{g(x, y)}{R^p} \exp \{ -j2\pi \hat{f}_{p0} R(\chi) \} \left(1 - \frac{l(\chi)}{\rho_0 \tan \theta_0} \right) H(\hat{f}_{p, moc}) \exp \{ -j2\pi \hat{f}_{p, moc} R(\chi) \} \quad (25)$$

$$\hat{f}_{p, moc} = \frac{\hat{f}_p + f_{p0} \frac{l(\chi)}{\rho_0 \tan \theta_0}}{1 - \frac{l(\chi)}{\rho_0 \tan \theta_0}} \quad (26)$$

Assuming that only the first order term in the motion perturbations matter, this can be approximated by (15).

XII. APPENDIX B

Solving (5) to first order in the motion perturbation, gives the following modification to the simple solution, (6)

$$\hat{\kappa} = f_1 + y_1 + y_2 + k_1 + l_1$$

$$f_1 = -\kappa_0 \frac{\kappa_0^2}{(y^2 + 1)} \frac{l(\kappa_0 + x)}{\rho_0 \tan \theta_0}$$

$$y^2 \left(\frac{\kappa_0^2}{y^2} - 1 \right)^2 \frac{l'(\kappa_0 - 1 x)}{\rho_0 \tan \theta_0} \quad (27)$$

$$y_1 = \frac{\kappa_0}{y} \Delta y (\kappa_0 - 1 x) \quad (28)$$

$$y_2 = - \frac{\kappa_0^2}{(y^2 + 1)} \frac{1}{y} \Delta y y'(\kappa_0 + x) \quad (29)$$

$$k_1 = \frac{\kappa_0^2}{(y^2 + 1)} \frac{3}{2} y k'(\kappa_0 + x) \quad (30)$$

$$l_1 = - \frac{\kappa_0^2}{(y^2 + 1)} \frac{3}{2} \frac{l'(\kappa_0 + x)}{y \tan \theta_0} \quad (31)$$

The individual contributions can be related to the physics of the problem. The f_1 term is a correction for the frequency shift caused by the first order motion compensation. The y_1 term is a correction of the azimuth chirp rate as the slant range is modified by the motion in the slant range plane. The y_2 , k_1 , and l_1 terms are corrections for the image skew that are implemented by the actual track not being parallel to the reference track, and the motion compensation applied to correct for it. It is noted that if the assumed motion is identical to the motion corrected for, $Ay = k$, then the y_2 and k_1 terms will be close to identical.

REFERENCES

- [1] W. M. Brown, "Synthetic aperture radar," *IEEE Transactions on Aerospace and Electronic Systems*, vol. AES-3, pp. 217-229, Mar. 1967. can be found in *Synthetic Aperture Radar*, ed. J. J. Kovaly.
- [2] J. C. Curlander and R. N. McDonough, *Synthetic Aperture Radar: Systems and Signal Processing*. Wiley, 1991.
- [3] J. J. Kovaly, *Synthetic Aperture Radar*. Artech House, 1976.
- [4] C. Elachi, *Spaceborne radar remote sensing: applications and techniques*. IEEE Press, 1988.
- [5] J. van Zyl, R. Carande, Y. Lou, T. Miller, and K. Wheeler, "The NASA/JPL full-frequency polarimetric airsar system," in *Proceedings of the International Geoscience and Remote Sensing Symposium, IGARSS'92*, Vol. 11, pp. 649-651, 1992.
- [6] R. S. Vickers, V. H. Gonzalez, and R. W. Picklin, "Results from a VHF impulse synthetic aperture radar," in *SPIE conference on Radar Sensor Technology*, vol. 1631, pp. 219-225, Apr. 1992.
- [7] H. Hellsten, L. Ulander, A. Gustavson, and B. Larsson, "Development of VHF CARABAS II SAR," in *SPIE conference on Radar Sensor Technology*, vol. 2747, Apr. 1996.
- [8] D. A. Giglio, "Overview of foliage/ground penetration and interferometric SAR experiments," in *SPIE conference on Radar Sensor Technology*, vol. 2230, Apr. 1994.
- [9] S. N. Madsen and H. A. Zebker, *Imaging radar interferometry*, ch. 17. American Society of Photogrammetry, 1996, in press.
- [10] H. Zebker and R. Goldstein, "Topographic mapping from interferometric SAR observations," *Journal of Geophysical Research*, vol. 91, no. B5, pp. 4993-4999, 1986.
- [11] E. Rodriguez and J. Martin, "Theory and design of interferometric synthetic aperture radars," *IEEE Proceedings*, vol. 139, pp. 147-159, 1992.
- [12] S. N. Madsen, H. A. Zebker, and J. Martin, "Topographic mapping using radar interferometry: Processing techniques," *IEEE Transactions on Geoscience and Remote Sensing*, vol. 31, pp. 246-256, Jan. 1993.
- [13] D. R. Stevens, I. G. Cumming, and A. I. Gray, "Options for airborne interferometric SAR motion compensation," *IEEE Transactions on Geoscience and Remote Sensing*, vol. 33, pp. 409-420, Mar. 1995.
- [14] S. N. Madsen, J. Martin, and H. A. Zebker, "Analysis and evaluation of the NASA/JPL TOPSAR across-track interferometric SAR," *IEEE Transactions on Geoscience and Remote Sensing*, vol. 33, pp. 383-391, Mar. 1995.

- [15] R. Bamler, "A comparison of range-doppler and wavenumber domain SAR focussing algorithms," *IEEE Transactions on Geoscience and Remote Sensing*, vol. 30, pp. 706-713, July 1992.
- [16] F. Rocca, "Synthetic aperture radar: A new application for wave equation techniques," tech. rep., Stanford Exploration Project Reports, 1987.
- [17] C. Cafforio, C. Prati, and F. Rocca, "SAR data focusing using seismic migration techniques," *IEEE Transactions on Aerospace and Electronic Systems*, vol. 27, pp. 194-207, Mar. 1991.
- [18] W. Carrara, S. Tummlala, and R. Goodman, "Motion compensation," in *SPIE conference on Radar Sensor Technology*, vol. 2487, pp. 13-23, Apr. 1995.
- [19] J. J. Bamberg and S. Sternberg, *A Course in Mathematics for Students of Physics: 2*. Press Syndicate of the University of Cambridge, 1990.

Søren Nørvang Madsen, M. Sc.E.E.'82, Ph.D.'86. From 1987 to 1989 he was an Associate Professor at the Electromagnetics Institute (TUD), working on the design of radar systems for mapping the Earth and other planets as well as the application of digital signal processing systems in radar systems. He was the initiator and project manager for the Danish Airborne synthetic aperture radar (SAR) program from its start until he left TUD. In 1990 he joined NASA's Jet Propulsion Labor-

tory, Pasadena. He first worked on geolocating SEASAT and SIR-B SAR data, then led the development of a SIR-C calibration processor prototype. He was also involved in the Magellan Venus radar mapper project. Since 1992 his main interest has been interferometric SAR systems. He has led the developments of the processing systems for the JPL/NASA across-track interferometer (TOPSAR) as well as the ERIM SAR system. Since 1993 he has split his time between JPL and TUD. At TUD he is heading the Danish Center for Remote Sensing (DCRS), and his work involves all aspects of SAR data processing, analysis, and applications, relating to the airborne Danish dual frequency polarimetric and interferometric SAR. At DCRS he is also a principal investigator for two ERS-1/-2 satellite SAR studies.